Microstructure, mechanical properties of dissimilar friction stir welded AA6063/AA5052 alloys, and optimization of process parameters using Box Behnken-TOPSIS approach

Desikan Sriram[1], Vittel Rao[2], Sivasundar Vijayakumar[3,4]*, Anusha Peyyala[5], Movva Naga Swapna Sri[5], Nidamanuri Srinivasa Rao[6], Nageswararao Cheepurupalli[7], Ram Subbiah[8]

[1]*Department of Mechanical Engineering, Indra Ganesan College of Engineering, Manikandam post, Trichy-620012, India*
[2]*Construction Mechanical Engineer, EPC Project, Adyard Abu Dhabi LLC, Abu Dhabi*
[3]*Department of Mechanical Engineering, Graphic Era Hill University, Dehradun-248002, Uttarakhand, India*
[4]*Department of Mechanical Engineering, Graphic Era Deemed to be University, Dehradun-248002, Uttarakhand, India*
[5]*Department of Mechanical Engineering, P V P Siddhartha Institute of Technology, Vijayawada, India*
[6]*Department of Mechanical Engineering, Shri Vishnu Engineering College for Women, Bhimavaram, India*
[7]*Department of Mineral Processing and Metallurgical Engineering, Faculty of Mines, Aksum University, Ethiopia*
[8]*Department of Mechanical engineering, Gokaraju Rangaraju Institute of Engineering and Technology, Hyderabad, India*

Abstract

AA6063 and AA5052 plates are welded together with the help of friction stir welding (FSW). Experiments are performed based on the Box-Behnken experimental design (BBD) because this design minimizes the number of experimental runs required and reduces the time and resources needed for experimentation. The four factors (Tool Rotational Speed (TR), Welding Speed (WS), Pin Depth (PT), and Pin Offset (PO)) are selected as input responses to perform welding operation. TOPSIS method is well-suited for situations where decisions must be made based on several conflicting criteria, making it applicable to evaluate welding factors on mechanical properties. The multi-response optimization for output responses uses the BBD-based TOPSIS method. The optimal combination for higher tensile strength, hardness, and lower wear rate is at TR1-WS2-PO1-PT2 condition, and the value of multi-optimized output responses are found to be 201.96 MPa, 90.5 HV, and 0.00329 $\mathrm{m^3\,N^{-1}\,m^{-1}}$, respectively.

K e y w o r d s: Friction Stir Welding (FSW), multi-response optimization, Box-Behnken experimental design (BBD), TOPSIS and SEM analysis

1. Introduction

Friction stir welding holds significant importance in the domain of metal joining procedures. This method is considered safe and cost-effective, facilitating the joining of materials typically categorized as non-weldable [1, 2]. The geometry of the tool, tool depth, and selection of material influence the quality of the joint. Furthermore, these parameters impact monitoring variables like forces, torque, and the temperature of both the workpiece and tool throughout the process [3–5]. Jayaseelan et al. [6] carried out FSW on AMC with SiC and ZrB_2 reinforcements and studied the influence of tool profiles and the

D/d ratio of the tool on the weld joint. The findings indicate that utilizing a threaded profile tool crafted with a D/d ratio produces weld joints with more strength. From microstructure examination, Al-10 % ZrB_2 and Al-10 % SiC plates demonstrate significant grain refinement, accompanied by a uniform distribution of precipitates. Jia et al. [7] studied the FSW of AA6061/AA5083 alloys, focusing on the importance of individual welding parameters. The impact of these welding factors on material mixing was examined using metallography and microhardness assessments. The study revealed insufficient material mixing at more traverse speeds, which causes void-type defects. Ghaffar et al. [8] presented a statistical

*Corresponding author: e-mail address: vijaysundarbe@gmail.com

analysis to forecast the mechanical properties of Al 1050 based on process parameters, including feed rate, number of passes, and tool shape. A central composite design incorporating four factors with five levels was employed. RSM was then applied to formulate regression models for predicting the responses UTS, elongation %, and hardness. Numerous scholars have focused on mathematical modeling, primarily optimizing the factors associated with FSW in metal alloys [9]. Kundu et al. [10] conducted an optimization process for FSW AA5083-H321. The Taguchi-GRA technique was established to identify solutions for the associated multi-objective optimization problem. Rathinasuriyan et al. [11] also offered the optimization process for FSW of 6061-T6 Al alloy with the help of the GRA technique. Tamjidy et al. [12] investigated dissimilar welded joints with FSW parameters, including tilt angle and tool offset, which were systematically modified to determine their impact on the mechanical characteristics of the joint. Optimization was determined by a multi-response optimization algorithm based on the biogeography optimization method. Sinha et al. [13] optimized FSWs for Al-Li alloy. Tool pin profile, welding preheating conditions, rotational speed, and welding speed were chosen for optimization using ANOVA and regression analysis. The findings indicated that the optimal welding conditions were a rotational speed of 1500 rpm, welding speed of 90 mm min^{-1}, cylindrical tool profile, and preheating at 80 ℃, resulting in a 5.32 % improvement in tensile strength and a 1.65 % reduction in tool wear rate. Kahhal and colleagues [14] conducted a multi-response optimization study on AA1050 A-H12 alloy, employing the RSM and a swarm optimization algorithm. Nosrati et al. [15] explored the double-side FSW of AA 2024-T6 using the CCD-RSM. Artificial neural networks were used to construct an intelligent relationship between parameters and responses. The ideal neural network was combined with the Whale Optimization Algorithm (WOA) to discover the best variables and produce desirable results. The study found that the tool pin's length (h) had the greatest contribution percentage to improving mechanical properties. Sahu et al. [16] investigated the impact of tool pin geometry on the FSW of marine-grade AA5083 to analyze the results, which revealed a joint efficiency of 75.67 % and a UTS of 212 MPa due to a rotating speed of 1,000 and a speed of welding of 28 mm min^{-1}. The GRA-Taguchi technique was used to optimize the 6061/SiC welded joint across many objectives. The welding input factors for analyzing mechanical properties included the tool pin profile, shoulder size, and plunge depth [35]. Chaudhary et al. [17] prepared FSW of Inconel 625 alloy using the Tungsten carbide tool. The Genetic Algorithm-based Taguchi design was employed to validate the experimental values. Experimental validation of the mathematical equation highlighted the useful-

ness of utilizing a rotating machine with a speed of 300 rpm, a welding speed of 115 mm min^{-1}, and a radial force of 18 kN to reach a maximum weld strength of 407 N mm^{-2}. Shojaefard et al. [18] employed a hybrid approach involving ANN and PSO methods to derive an optimal combination for conflicting properties, specifically UTS and hardness. Pankaj et al. [19] investigated the effect of temperature distribution and force analysis for H36 steel/AISI 1008 steel.

Gupta et al. [20] utilized a hybrid optimization method, combining GRA with PCA for multi-response optimization. The application of PCA in this optimization method was noted for its significant effectiveness across different manufacturing processes. Premnath et al. [21] used an advantageous approach to improve the mechanical characteristics of aluminum-SiC nanocomposites made via the FSP process. Their research included an evaluation of the microstructure of both manufactured and worn surfaces.

Based on the above reviews, it is apparent that only a limited number of researchers have directed their attention to welding dissimilar Al alloys through FSW. Previous investigations indicate that numerous researchers have explored various multi-criteria decision-making techniques, including Taguchi, GRA, PCA, PSO, AHP, CCD, fuzzy AHP, and fuzzy PCA, independently or in combination within the welding processes. Nevertheless, a gap exists in exploring a hybrid approach combining Box-Behnken design with TOPSIS for friction stir welding (FSW) operations on AA6063/AA5052 plates. The current study aimed to optimize the process variables tool rotational speed, welding speed, pin depth, and pin offset in the FSW of AA6063/AA5052 plates. Tensile strength, hardness, and wear rate were chosen as output response variables for analysis. The experiments use the Box-Behnken design, and mathematical models are established to relate responses to input parameters. The adequacy of the model is assessed using S/N ratio and ANOVA. The conditions for multi-criteria optimization of process parameters are predicted using the Box-Behnken design-based TOPSIS method. A confirmatory study is conducted to validate the results of the optimization. Additionally, optical microscope and SEM analyses are performed on the fractured surfaces to examine the failure mode, grain structure, and surface condition of the joints.

2. Materials and methods

AA6063 and AA5052 aluminum alloys are suitable for wide aerospace and automotive engineering applications. The chemical elements of both alloys are presented in Table 1.

Both alloys are in plate form with dimensions of 5 mm thick, 180 mm length & 40 mm width, and un-

T a b l e 1. Chemical composition AA6063 and AA 5052 alloys (in wt.%)

Material	Mn	Fe	Mg	Si	Zn	Cr	Cu	Al
AA6063	0.18	0.9	1.7	0.6	0.45	0.13	0.13	Bal
AA5052	1.8	0.55	3.1	0.25	0.15	0.27	0.18	Bal

T a b l e 2. FSW factors

Factors	Units	Low	Medium	High
TR	Rpm	800	900	1000
WS	mm min^{-1}	60	80	100
PO	mm	0.5	0.7	0.9
PT	mm	0.2	0.3	0.4

T a b l e 3. Experimental results for measured TS, HN, and WR of used alloys

Run	TR (Rpm)	WS (mm min^{-1})	PO (mm)	PT (mm)	TS (MPa)	HN (HV)	WR (m^3 N^{-1} m^{-1})
1	900	60	0.7	0.4	195.21	88.5	0.0056
2	800	80	0.7	0.2	195.84	79.5	0.00651
3	900	80	0.5	0.4	192.1	81.2	0.00539
4	900	100	0.7	0.4	181.94	84.3	0.00674
5	1000	60	0.7	0.3	200.4	78.6	0.0074
6	900	80	0.5	0.2	201.96	90.5	0.00329
7	900	80	0.9	0.2	198.24	85.3	0.00272
8	900	60	0.9	0.3	197.33	84.6	0.00357
9	900	100	0.9	0.3	195.04	79.5	0.00396
10	1000	100	0.7	0.3	174.3	81.2	0.00482
11	1000	80	0.7	0.2	185.41	83.6	0.00583
12	800	100	0.7	0.3	174.79	91.2	0.00501
13	800	80	0.7	0.4	176.08	77.5	0.01005
14	800	60	0.7	0.3	176.79	88.2	0.01071
15	900	100	0.5	0.3	171.38	93.5	0.01078
16	900	80	0.7	0.3	202.39	90.6	0.01011
17	800	80	0.9	0.3	201.26	82.6	0.01066
18	1000	80	0.5	0.3	195.29	87.3	0.01005
19	800	80	0.5	0.3	173.65	90.4	0.01191
20	900	60	0.7	0.2	198.03	93.5	0.01282
21	1000	80	0.7	0.4	185.61	84.3	0.0117
22	900	60	0.5	0.3	201.21	89.5	0.0067
23	900	100	0.7	0.2	182.29	79.3	0.00736
24	1000	80	0.9	0.3	178.06	83.9	0.01103
25	900	80	0.9	0.4	180.76	87.8	0.00945

derwent butt welding utilizing Friction Stir Welding. The welding operation is conducted on a sturdy milling machine arranged in a butt configuration. To ensure secure positioning and clamping of the tool and workpieces during the joining process, a designed tool adapter and a work fixture were affixed to the milling machine [22]. The tool employed in this process is made of H13 steel, featuring a pin diameter of 6 mm and a pin length of 3 mm (Figs. 1a,b). A four-factor, three-level factorial design is utilized to optimize the conditions of the friction stir welding parameters. The selected independent factors included Tool Rotational Speed (TR), Welding Speed (WS), Pin Offset (PO), and Pin Depth (PT), each set at –1, 0, and +1 levels, as outlined in Table 2. 25 experiments were executed according to the trial plan of Box-Behnken design to investigate its impact on dependent variables with the help of *Design-Expert software-13* [23]. These FSW experiments were performed to analyze the outputs of Tensile Strength (TS), Hardness (HN), and Wear Rate (WR) in Table 3. Tensile tests were prepared per ASTM-E8 standards, and subsequent tests were conducted via a universal machine at room temperature. For hardness measurements, a Brinell micro-

hardness tester was employed at a 25 mm length with a 30-second dwell time under a 150 g load. Wear tests follow ASTM G99 standards utilizing a Pin on Disc.

3. Results and discussion

3.1. Impact of welding parameters on the tensile strength

Design Expert software generates 3D response surface graphs demonstrating the effect of four variables on the TS of the FSW joint, as illustrated in Figs. 2a–f. In Fig. 2a, the 3D surface plot reveals the relationship between TS and TR and WS. Analysis of the figure indicates that lower TS occurs at a lower TR of 800 rpm

and WS of 60 mm min^{-1}, while higher TS is achieved at TR of 900 rpm and WS of 80 mm min^{-1}. From the Fig. 2b, the 3D surface plot represents the interplay between TR and PO. Initially, the TS value decreases at a PO of 0.5 mm, but as the PO value gradually increases to 0.7 mm, it increases TS. Figure 2c explains the 3D plot of tensile strength concerning TR and PT. The results indicate that the lowest TS is detected at TR of 800 rpm and PT of 0.4 mm, while the higher TS is noted at TR of 900 rpm and PT of 0.3 mm. This implies an indirect proportionality between pin depth and the increment of TS. In Fig. 2d, the 3D plot shows the connection between Tensile Strength and WS and PO. The lowest TS is observed at WS of 100 mm min^{-1} and PO of 0.5 mm, while the higher TS is noticed at WS of 60 mm min^{-1} & PO of 0.5 mm.
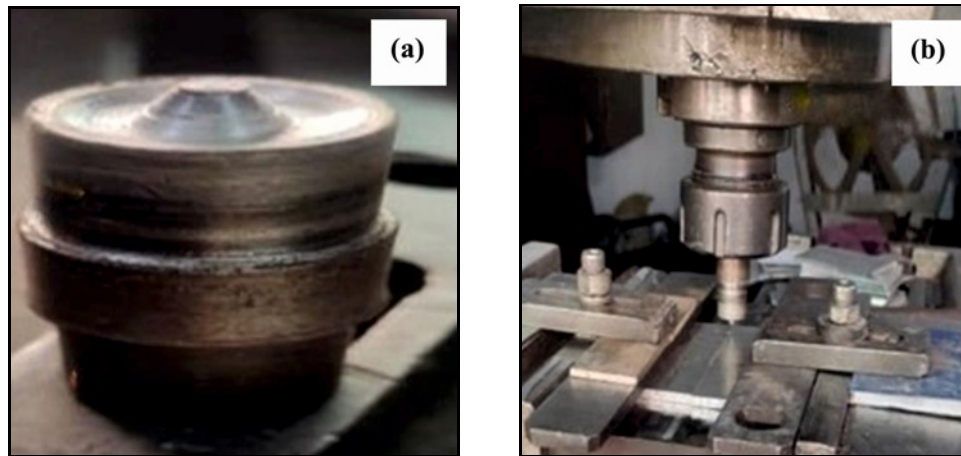

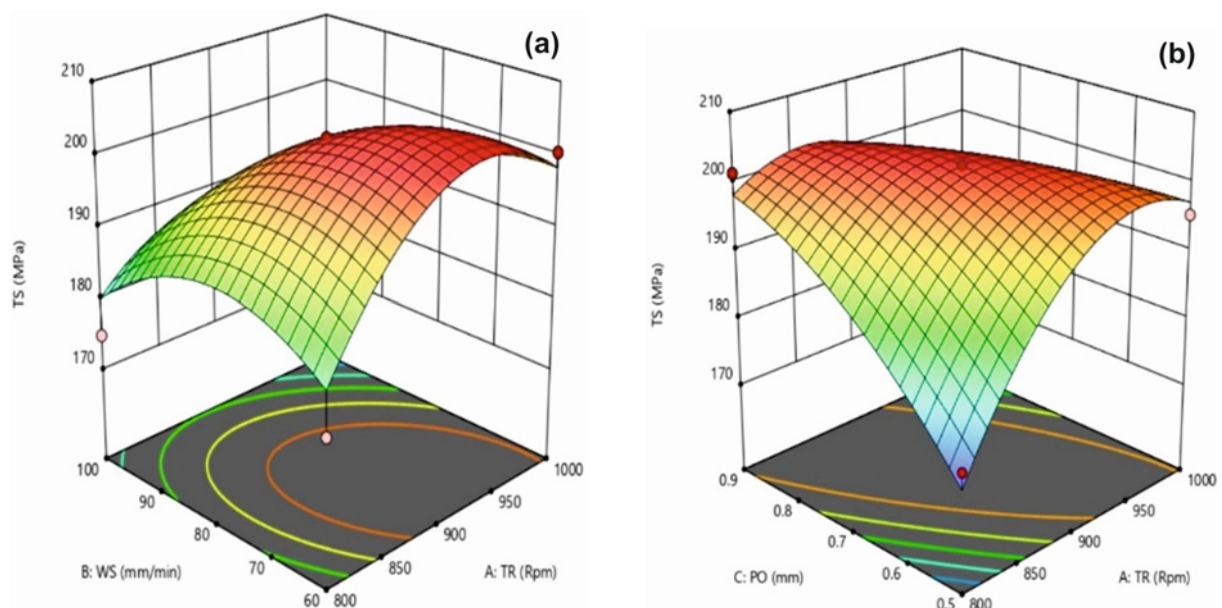Fig. 1. (a) FSW tool, (b) Al plates joint.

Fig. 2a,b. 3D surface plots for tensile strength versus FSW factors: (a) TR and WS, (b) TR and PO.
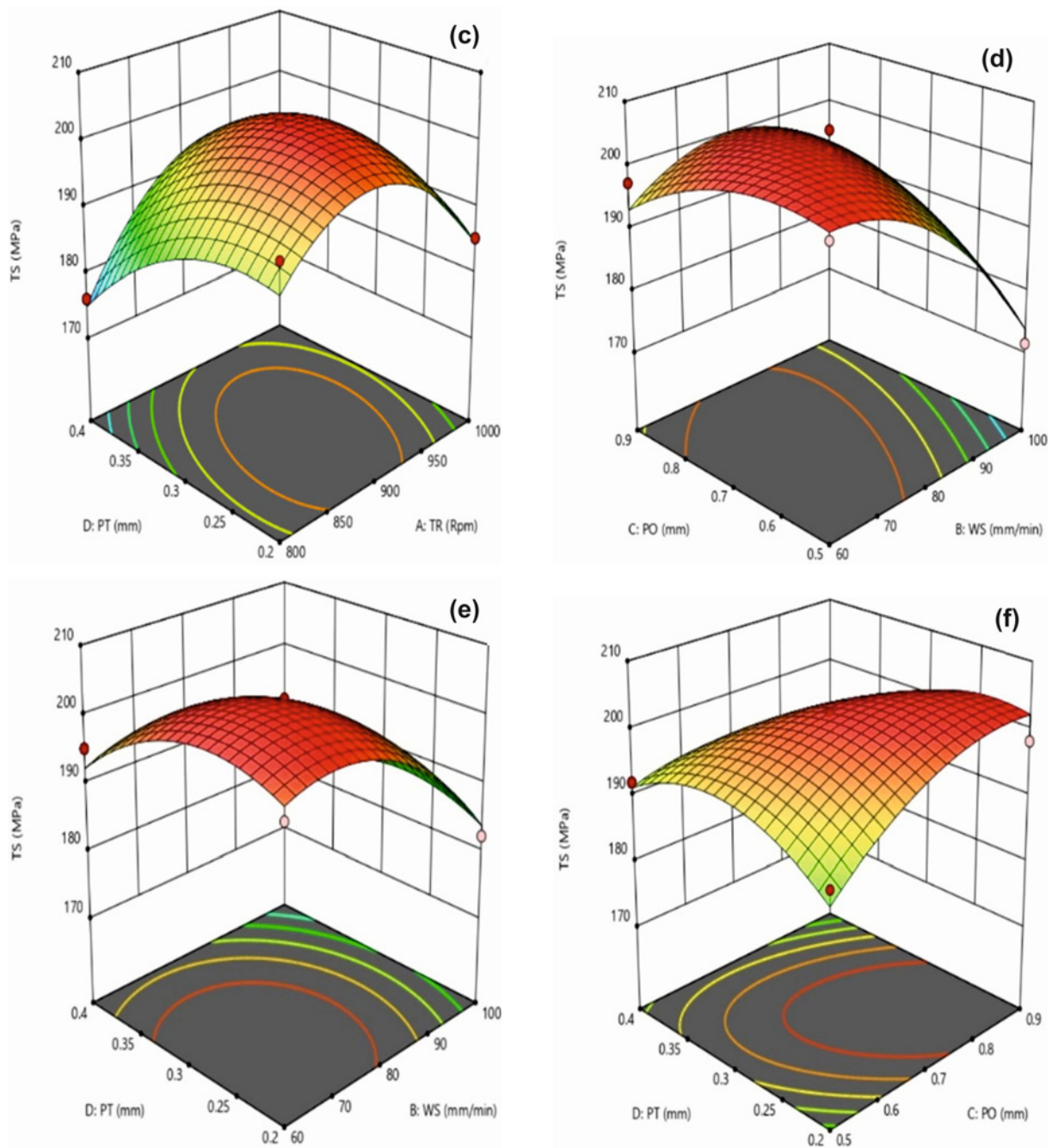
Fig. 2c–f. 3D surface plots for tensile strength versus FSW factors: (c) TR and PT, (d) WS and PO, (e) WS and PT, and (f) PO and PT.

Figures 2e,f similarly describe the 3D surface plots of tensile strength versus welding speed and pin depth (WS & PT) and pin offset and pin depth (PO & PT), respectively.

3.2. Optical microstructure analysis on FSW plates

The welded specimens were inspected with the help of an Olympus microscope to analyze the microstructural detail, and the specimens were etched with

Keller's etchant to deliver clear images. The structure of AA5052 and AA6063 is described in Figs. 3a,b in that the clear distinction in grain structure and size variations can be seen.

Figure 4 exhibits the optical microstructure of the AA6063 and AA5052 plates for the experimental run: 16 with process factors of 900 rpm, 80 mm min^{-1}, 0.7 and 0.3 mm, respectively. During the stirring stage, a tool embedded in a spinning probe travels the length of the plates to be welded, which causes a nugget zone due to entanglement between the tool and the
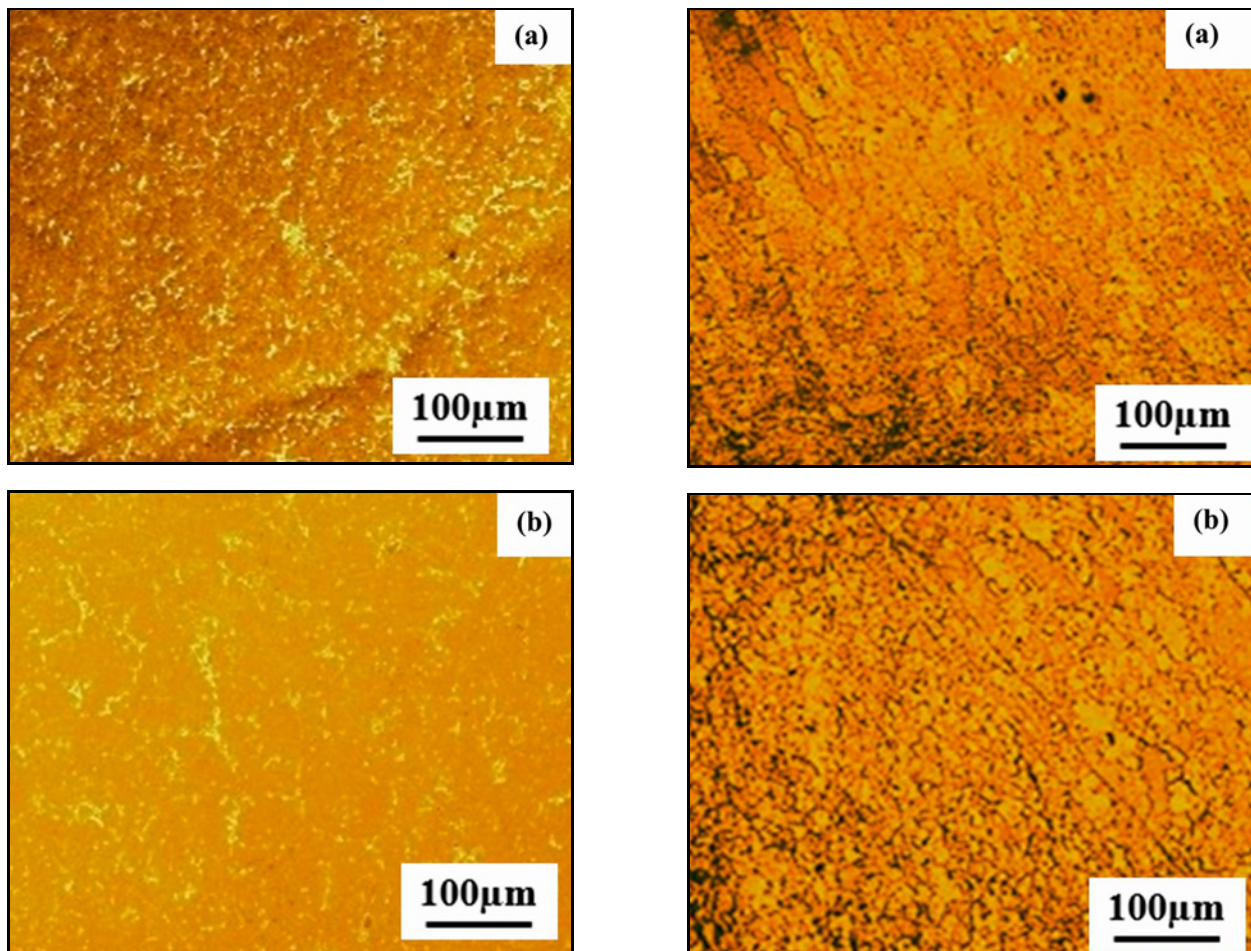
Fig. 3. Microstructure of the base metals: (a) AA 5052 and (b) AA6063.

Fig. 4. Optical microstructure of the (a) HAZ, (b) TMAZ, (c) Nugget zone produced at Experiment run 16.

workpieces. TMAZ is created by the force generated between the shoulder of the tool and the top plates surface, as well as the contact between the adjacent metal and the tool edges [25]. Compared to the NZ, the material experiences less strain and a lower strain rate at the TMAZ. The pancake-shaped grains along the interface of the NZ and TMAZ are elongated and bent, showing that FSW causes substantial deformation in the elongated grains [26, 27]. Additionally, the grain structures at the HAZ closely resemble those of the base metals [28, 29].

The microstructure of the HAZ is presented in Fig. 4a. Identifying differences in grain structure between the base metals and HAZ proved challenging due to the low thermal sensitivity.

Figure 4b depicts the microstructure of the TMAZ, revealing highly elongated grains of the Al alloy without recrystallization. Additionally, the Nugget Zone (NZ) microstructure is distinct from the distorted zone of TMAZ, exhibiting plastic deformation without recrystallization. The microstructure of the NZ is shown in Fig. 4c. The nugget zone experiences severe plas-
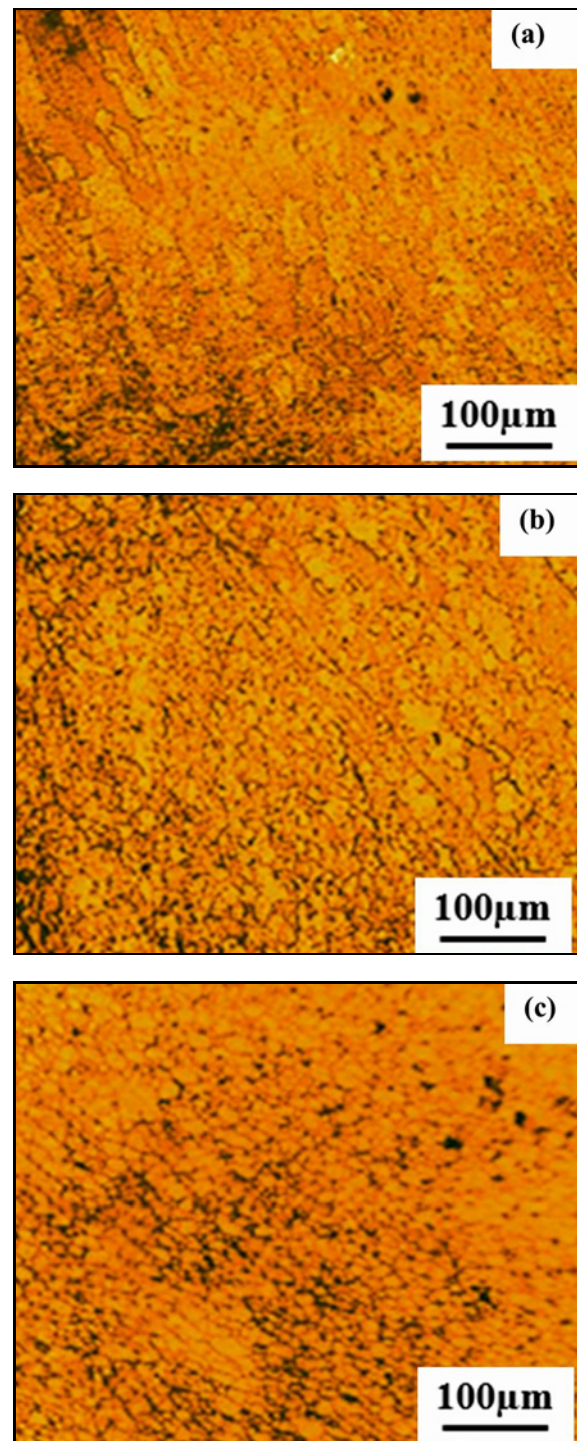
tic deformation, resulting in the development of fine-equiaxed recrystallized grains. Frictional heat generated during welding plays an important role in grain refining within the area of welding, potentially increasing weld strength. Fusion welding flaws such as pores and cavities are negligible in the weld zone [30].
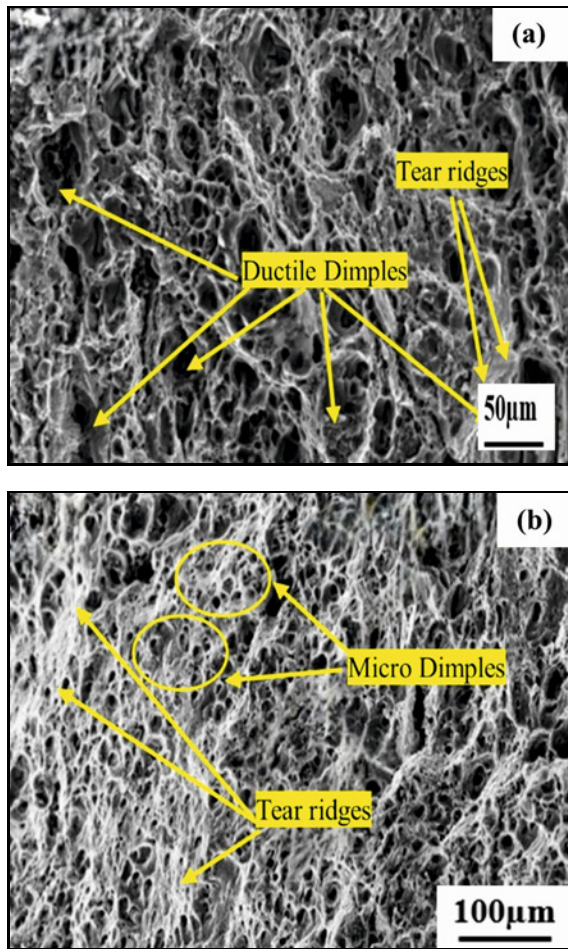
Fig. 5. Fractured surfaces of welded joints for Experiment Run 19 and Experiment Run 16.

T a b l e 4. *SN* ratio for TS

Level	TR	WS	PO	PT
1	−45.24	−45.78	−45.44	−45.65
2	−45.62	−45.51	−45.42	−45.46
3	−45.40	−45.10	−45.65	−45.35
Delta	0.39	0.69	0.23	0.30
Rank	2	1	4	3

Fig. 6. SN plot for TS.

3.3. Investigation of SEM evaluation on ruptured specimens from the tensile test

Analyzing the fracture surfaces of an FSW joint between AA6063 and AA5052 involves examining the fractured surfaces to gain insights into the failure mechanisms and features of the joint. These surfaces offer valuable information about microstructural features, material flow, and weld integrity. Figures 5a,b illustrate the fractured surfaces of welded AA6063 and AA5052 joints for Experiment Run 19 (800 rpm, $80\,\mathrm{mm\,min^{-1}}$, 0.5 mm & 0.3 mm) and Experiment Run 16 (900 rpm, $80\,\mathrm{mm\,min^{-1}}$, 0.7 mm & 0.3 mm), respectively. It was noticed on the ruptured surface that large dimples or ductile dimples were present on the right end corner (Fig. 5a). The major cause of the fracture is revealed to be a load imbalance, with the failure regulated by a combination of microvoids. As the strain grew in the tensile test, these micro gaps prolonged and eventually formed a single fracture surface. The pres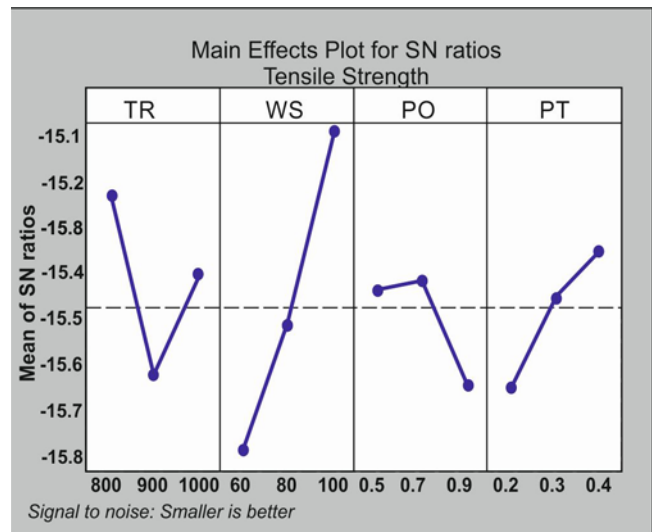ence of diverse compound particles in the joint's HAZ frequently resulted in dimple development, attributed to considerable precipitated coarsening during welding. Significant changes in the fracture surface appearance are noticeable along the directions of the welded specimens. In the weld direction, the fractured samples of composites displayed a ductile fracture characterized by dispersed micro dimples and tearing ridges (Fig. 5b). This behavior can be ascribed to temperature distribution, material flow, and the presence of a fine equiaxed grain structure.

3.4. Analysis of output responses using S/N ratio and ANOVA

Tensile strength is examined by analyzing the S/N ratio and ANOVA techniques in *MINITAB software*. Table 4 presents the mean S/N ratio of tensile strength at various levels of the input process variables. Additionally, the table includes the ranking of each process parameter, indicating the degree of sensitivity of tensile strength to these process factors.

Table 4 indicates that the welding speed holds the top rank assigned as 1, signifying the high sensitivity of TS. As depicted in Fig. 6, the optimal combination for maximizing TS is TR2-WS1-PO3-PT1, corre-

Table 5. ANOVA result for TS

Source	DF	SS	SS	MS	F	P
TR	2	0.6541	0.8830	0.4415	2.58	0.107
WS	2	1.5940	1.7768	0.8884	5.19	0.018
PO	2	0.1348	0.2427	0.1214	0.71	0.507
PT	2	0.4600	0.4600	0.2300	1.34	0.289
Residual Error	16	2.7398	2.7398	0.1712	–	–
Total	24	5.5827	–	–	–	–

Table 7. ANOVA result for HN

	DF	Seq SS	SS	MS	F	P
TR	2	0.5693	0.6723	0.3361	1.42	0.0270
WS	2	0.1755	0.2470	0.1235	0.52	0.0603
PO	2	0.7769	0.7102	0.3551	1.50	0.0252
PT	2	0.4343	0.4343	0.2172	0.92	0.0519
Residual Error	16	3.7793	3.7793	0.2362		
Total	24	5.7354				

Table 6. S/N ratio for HN

Level	TR	WS	PO	PT
1	−38.56	−38.79	−38.95	−38.60
2	−38.76	−38.57	−38.54	−38.70
3	−38.39	−38.55	−38.48	−38.47
Delta	0.36	0.24	0.48	0.23
Rank	2	3	1	4

Table 8. S/N ratio for WR

Level	TR	WS	PO	PT
1	41.17	42.89	42.71	44.98
2	44.27	42.37	42.33	42.39
3	41.90	44.30	44.56	42.15
Delta	3.10	1.94	2.24	2.83
Rank	1	4	3	2

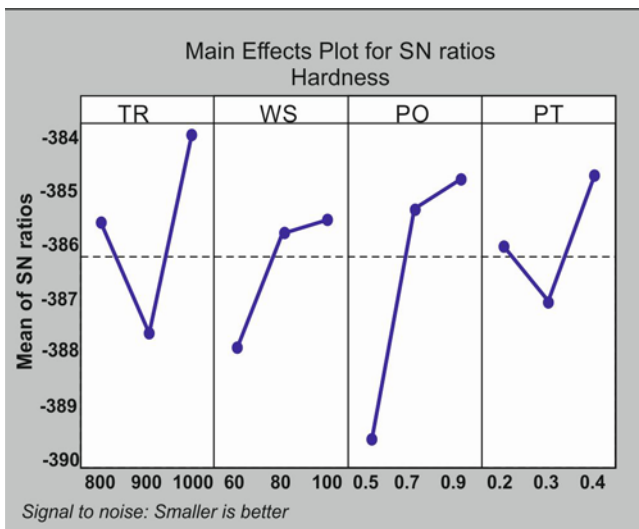

Fig. 7. SN plot for HN.

Fig. 8. SN plot for WR.

sponding to TR at level 2 (900 rpm), WS at level 1 (60 mm min^{-1}), PO at level 3 (0.9 mm), and PT at level 1 (0.2 mm). The factors among the process parameters that significantly impact TS are identified based on F and P values. As per Table 5, it is clear that WS exhibits a P-value lower than 0.05.

Table 6 displays the S/N ratio of Hardness (HN) across different levels of factors. Additionally, the table presents the ranking of each process factor, indicating the degree of sensitivity of hardness. Analysis of Table 6 reveals that PO holds the top rank (rank 1), signifying the high sensitivity of HN to changes in
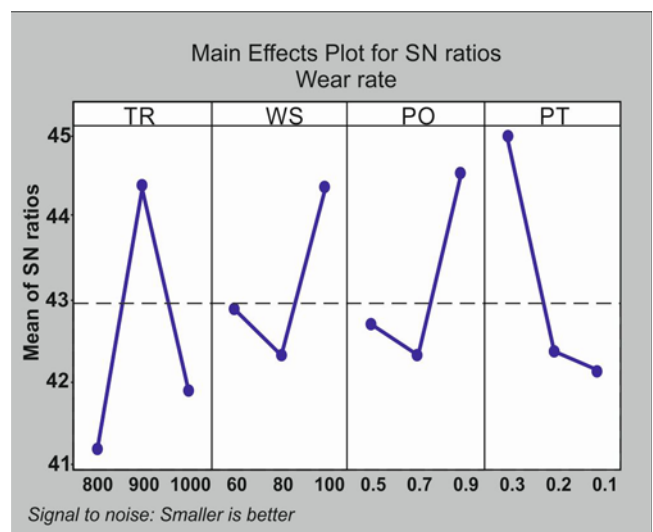
pin offset. According to Fig. 7, the optimal combination for maximizing Total Strength (TS) is TR2-WS1-PO3-PT2, corresponding to TR at level 2 (900 rpm), WS at level 1 (60 mm min^{-1}), PO at level 1 (0.5 mm), and PT at level 2 (0.3 mm). The ANOVA results in Table 7 identify the process factors significantly affecting HN based on F and P values. It is evident that the P-value for PO is 0.0252, which is less than 0.05. Therefore, PO is the most significant process variable compared to others.

Table 8 illustrates the S/N ratio of wear rate (WR) across different levels of FSW process parameters. Ta-

Table 9. ANOVA for WR

Source	DF	SS	SS	MS	F	P
TR	2	48.331	3.117	1.558	0.10	0.0907
WS	2	7.439	21.713	10.856	0.69	0.0518
PO	2	14.427	26.839	13.420	0.85	0.0446
PT	2	39.109	39.109	19.555	1.24	0.0317
Residual Error	16	252.979	252.979	15.811	–	–
Total	24	362.285	–	–	–	–

ble 8 highlights that TR holds the top rank (rank 1), suggesting high sensitivity of WR. As depicted in Fig. 8, the optimal combination for influencing WR is TR1-WS2-PO2-PT3, representing TR at level 1 (800 rpm), WS at level 2 (80 mm min^{-1}), PO at level 2 (0.7 mm), and PT at level 3 (0.4 mm). The ANOVA results in Table 9 identify the process parameters significantly affecting WR based on P-values. The P-values for PT and PO are 0.0317 and 0.0446, both less than 0.05. Therefore, PO and PT emerge as the most significant process parameters compared to other factors.

3.4.1. TOPSIS analysis

TOPSIS is a nonparametric method utilized to choose the optimal alternative among various alternatives. In this method, vector calibration is applied to remove the units of standard functions. The technique aims to identify the most favorable solution by considering its proximity to the positive and negative ideal solution [31, 32]. The six steps are used in the TOPSIS analysis to integrate the three responses (TS, HN, and WR) into a single response.

Step 1: The decision matrix is to be established, i.e., $i = 1, 2, 3, \ldots, n$, and alternative index $j = 1, 2, 3, \ldots, q$. The entries in the decision matrix correspond to the criteria values i associated with alternative j:

$$\text{Decision matrix} = \begin{bmatrix} b_{11} & b_{12} & \ldots & b_{1q} \\ b_{21} & b_{22} & \ldots & b_{2q} \\ \ldots & \ldots & \ldots & \ldots \\ b_{n1} & b_{n2} & \ldots & b_{nq} \end{bmatrix}. \quad (1)$$

Step 2: The normalized decision matrix (ND) represents the combination of possibilities in the matrix of assessments 'b' that must be translated to the normalized scale. The conditions used for increasing the

Table 10. Normalized and weighted normalized values

Exp. No.	Normalized			Weighted Normalized		
	TS	HN	WR	TS	HN	WR
1	0.237446	0.238039	0.167139	0.083106	0.083314	0.058499
2	0.238213	0.213832	0.194299	0.083374	0.074841	0.068005
3	0.233664	0.218404	0.160872	0.081782	0.076441	0.056305
4	0.221305	0.226742	0.201164	0.077457	0.07936	0.070407
5	0.243759	0.211411	0.220863	0.085316	0.073994	0.077302
6	0.243759	0.243418	0.098194	0.085316	0.085196	0.034368
7	0.241132	0.229432	0.081182	0.084396	0.080301	0.028414
8	0.240025	0.227549	0.106551	0.084009	0.079642	0.037293
9	0.23724	0.213832	0.118191	0.083034	0.074841	0.041367
10	0.212012	0.218404	0.143859	0.074204	0.076441	0.050351
11	0.225526	0.224859	0.174004	0.078934	0.078701	0.060901
12	0.212608	0.245301	0.14953	0.074413	0.085855	0.052335
13	0.214177	0.208452	0.299955	0.074962	0.072958	0.104984
14	0.215041	0.237232	0.319654	0.075264	0.083031	0.111879
15	0.20846	0.251487	0.321743	0.072961	0.08802	0.11261
16	0.24618	0.243687	0.301746	0.086163	0.08529	0.105611
17	0.244805	0.22217	0.318161	0.085682	0.07776	0.111357
18	0.237544	0.234811	0.299955	0.08314	0.082184	0.104984
19	0.211222	0.243149	0.355469	0.073928	0.085102	0.124414
20	0.240877	0.251487	0.382629	0.084307	0.088021	0.13392
21	0.225769	0.226742	0.349202	0.079019	0.07936	0.122221
22	0.244745	0.240729	0.19997	0.085661	0.084255	0.06999
23	0.221731	0.213294	0.219669	0.077606	0.074653	0.076884
24	0.216586	0.225666	0.329205	0.075805	0.078983	0.115222
25	0.21987	0.236156	0.282047	0.076954	0.082655	0.098717

T a b l e 11. TOPSIS Ideal solution and Relative closeness coefficient

Exp. No.	SE_i^+	SE_i^-	RC_i	Rank
1	0.03060	0.06749	0.68802	8
2	0.04182	0.05739	0.57849	10
3	0.03051	0.06877	0.69264	7
4	0.04375	0.05457	0.55501	12
5	0.05087	0.04872	0.48920	13
6	0.00664	0.09171	0.93245	1
7	0.00792	0.09696	0.92450	2
8	0.01240	0.08807	0.87662	3
9	0.01874	0.08368	0.81701	4
10	0.02754	0.07416	0.72921	6
11	0.03456	0.06405	0.64952	9
12	0.02674	0.07324	0.73255	5
13	0.07884	0.01953	0.19856	18
14	0.08432	0.01625	0.16154	22
15	0.08522	0.01914	0.18337	20
16	0.07725	0.02608	0.25237	16
17	0.08358	0.01885	0.18405	19
18	0.07685	0.02380	0.23643	17
19	0.09682	0.01218	0.11176	24
20	0.10552	0.02112	0.16676	21
21	0.09448	0.00908	0.08771	25
22	0.04175	0.05702	0.57729	11
23	0.05100	0.04779	0.48372	14
24	0.08789	0.01135	0.11440	23
25	0.07111	0.02775	0.28075	15

TS and HN and decreasing the WR is:

$$t_{ij} = \frac{b_{ij}}{\sqrt{\sum_{i=1}^{n} b_{ij}^2}}. \tag{2}$$

Step 3: The weight decision matrix (WD) is calculated by keeping the weights of every response W_i (i.e., TS, HN, and WR) allotted equally and considered as 0.35:

$$WD = u_{ij} = W_i t_{ij}. \tag{3}$$

Step 4: A positive ideal solution that enhances the benefit and lowers the cost criteria, and a negative ideal solution that decreases the benefit while increasing the cost criteria:

$$a^+ = \left(a_1^+, a_2^+, \ldots, a_n^+\right) \quad \text{for max values,} \tag{4}$$

$$a^- = \left(a_1^-, a_2^-, \ldots, a_n^-\right) \quad \text{for min values.} \tag{5}$$

Step 5: The separation process is determined by separating different changes from negative & positive ideal solutions by using the below Eqs. (6), (7):

$$SE_i^+ = \sqrt{\sum_{j=1}^{N} \left(a_{ij} - a_j^+\right)^2}, \tag{6}$$

$$SE_i^- = \sqrt{\sum_{j=1}^{N} \left(a_{ij} - a_j^-\right)^2}. \tag{7}$$

Step 6: Find relative closeness coefficient RC_i values:

$$RC_i = \frac{SE_i^-}{SE_i^+ + SE_i^-}. \tag{8}$$

3.5. Confirmation test results

The confirmation trial is executed to validate the optimized outcomes after evaluating the optimal parameters. Equation (9) was applied to estimate the optimal values for Total Strength (TS), Hardness (HN), and Wear Rate (WR), respectively:

$$\$ = \mu_m + \sum_{i=1}^{q} (\mu_i - \mu_m), \tag{9}$$

where μ_m is the overall closeness coefficient value, q is the No. of controlled factors, and μ_i is the closeness coefficient at optimal conditions (Table 11). The BBD-TOPSIS method determined that the optimal combination was TR1-WS2-PO1-PT2. An experiment was conducted under this optimal condition (TR1-WS2--PO1-PT2), resulting in the following values: tensile strength of 201.96 MPa, hardness of 90.5 HV, and a

T a b l e 12. Confirmation test results

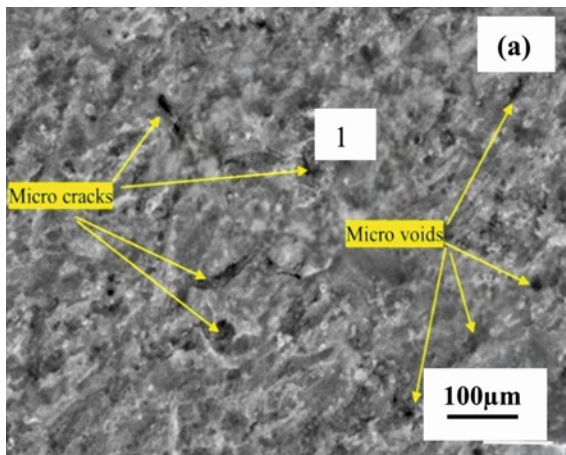| | Initial parameters | Optimal parameters | |
		Prediction	Experiment
Level	TR1-WS2- PO1-PT2	TR2-WS2-PO1-PT1	TR2-WS2-PO1-PT1
Tensile strength (MPa)	173.65	–	201.96
Hardness HV	90.4	–	90.5
Wear rate (m^3 $N^{-1}m^{-1}$)	0.01191	–	0.00329
Relative closeness coefficient	0.11176	0.8594	0.93245
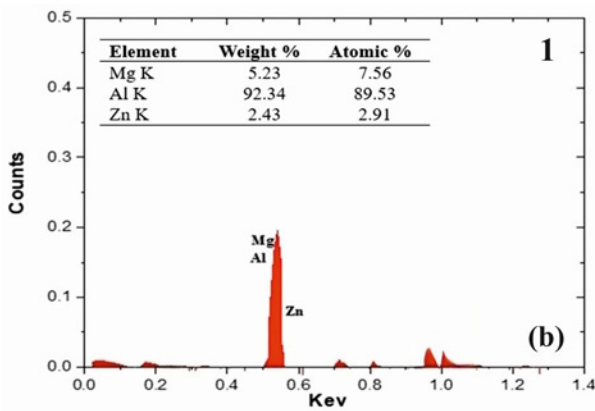
Fig. 9. Optimal condition TR1-WS2-PO1-PT2 sample: (a) SEM, (b) EDS.

wear rate of 0.00329 m^3 N^{-1} m^{-1}. The relative closeness coefficient at the initial process parameters and the final combination were 0.11176 and 0.93245, respectively. Table 12 presents all calculated values for both the initial and optimal runs. The observed improvement in the preference value for the ideal solution was determined to be 0.82069. Therefore, the results from the confirmation test indicate successful optimization.

Figure 9a displays the SEM images of the fracture surface for the optimal condition sample TR1--WS2-PO1-PT2, revealing the presence of smaller dimples indicative of superior joint ductility. This heightened ductility contributes to increased elongation and strength, primarily attributed to the smaller grain size in the nugget zone compared to the HAZ and TMAZ. Precipitate particles, predominantly comprising Mg, Zn, Mn, Cu, and Si compounds from the solid solution of the matrix, were possibly observed at the corner of the nugget zone. Figure 9b presents the EDS analysis of precipitated particles in the AA6063/AA5052 joint for the TR1-WS2-PO1-PT2 sample. The EDS results at point 1 reveal that the precipitates are predominantly composed of Mg-Zn compounds, namely $MgZn_2$, with the corresponding weight and atomic percentages displayed in Fig. 9b.

4. Conclusions

AA6063 and AA5052 alloys are welded through the FSW procedure with four welding factors. The experiments are conducted using the Box-Behnken experimental design. BBD-TOPSIS technique for multi-response optimization can easily optimize the output responses. The following decisions are made based on the obtained results:

– The optimal configuration for single-response optimization involves Tool Rotational Speed (TR) set at 900 rpm, Welding Speed (WS) at 60 mm min^{-1}, Pin Offset (PO) at 0.9 mm, and Pin Depth (PT) at 0.2 mm. This combination yields the highest tensile strength.

– The process variables for optimizing the hardness are TR2-WS1-PO3-PT2, corresponding to TR of 900 rpm, WS of 60 mm min^{-1}, PO of 0.9 mm, and PT of 0.3 mm. The optimal process variables for minimizing wear rate are TR1-WS2-PO2-PT3, with TR of 800 rpm, WS of 80 mm min^{-1}, PO of 0.7 mm, and PT of 0.4 mm.

– The best process parameters for multi-response optimization are TR1-WS2-PO1-PT2, suggesting TR of 800 rpm, WS of 80 mm min^{-1}, PO of 0.5 mm, and PT of 0.3 mm. This results in a higher tensile strength of 201.96 MPa, a higher hardness of 90.5 HV, and the lowest wear rate of 0.00329 m N^{-1} m^{-1}.

– The SEM analysis of the fracture surface in the

multi-response optimization sample reveals smaller dimples. These dimples indicate enhanced joint ductility, signifying superior mechanical performance in the welded joint. The EDS analysis of precipitated particles in the AA6063/AA5052 joint for the optimization sample indicates that the precipitates at point 1 consist primarily of Mg-Zn compounds in the form $MgZn_2$.

References

[1] R. S. Mishra, Z. Y. Ma, Friction stir welding and processing, Mater. Sci. Eng. R 50 (2005) 1–78. https://doi.org/10.1016/j.mser.2005.07.001

[2] D. Jacquin, G. Guillemot, A review of microstructural changes occurring during FSW in aluminium alloys and their modelling, J. Mater. Process. Technol. 288 (2021) 116706. https://doi.org/10.1016/j.jmatprotec.2020.116706

[3] N. Balasubramanian, B. Gattu, R. S. Mishra, Process forces during friction stir welding of aluminium alloys, Sci. Technol. Weld. Join. 14 (2009) 141–145. https://doi.org/10.1179/136217108X372540

[4] A. D'Orazio, A. Forcellese, M. Simoncini, Prediction of the vertical force during FSW of AZ31 magnesium alloy sheets using an artificial neural network-based model, Neural. Comput. Appl. 31 (2019) 7211–7226. https://doi.org/10.1007/s00521-018-3562-6

[5] S. Karumuri, B. Haldar, A. Pradeep, S. A. K. Karanam, M. N. S. Sri, P. Anusha, N. Sateesh, R. Subbiah, S. Vijayakumar, Multi-objective optimization using Taguchi based grey relational analysis in friction stir welding for dissimilar aluminium alloy, Int. J. Interact. Des. Manuf. 18 (2024) 1627–1644. https://doi:10.1007/s12008-023-01529-9

[6] P. Jayaseelan, T. V. Christy, S. J. Vijay, R. Nelson, Effect of tool material, profile and D/d ratio in friction stir welding of aluminium metal matrix composites, Mater. Res. Express. 6 (2019) 096590. https://doi:10.1088/2053-1591/ab30b1

[7] H. Jia, K. Wu, Y. Sun, F. Hu, G. Chen, Evaluation of axial force, tool torque and weld quality of friction stir welded dissimilar 6061/5083 aluminum alloys, CIRP J. Manuf. Sci. Technol. 37 (2022) 267–277. https://doi.org/10.1016/j.cirpj.2022.02.003

[8] A. Abdel Ghaffar Abdel Maboud, N. A. El-Mahallawy, S. H. Zoalfakar, Process parameters optimization of friction stir processed Al 1050 aluminum alloy by response surface methodology (RSM), Mater. Res. Express. 6 (2018) 026527. https://doi:10.1088/2053-1591/aaed7c

[9] S. F. Raza, M. Amjad, M. S. Habib, N. Ahmed, F. Riaz, Investigating the welding parameters in friction stir welding of yellow brass 405-20, Appl. Sci. 13 (2023) 2433. https://doi:10.3390/app13042433

[10] J. Kundu, H. Singh, Friction stir welding: multi-response optimisation using Taguchi-based GRA, Prod. Manuf. Res. 4 (2016) 228–241. https://dx.doi.org/10.1080/21693277.2016.1266449

[11] C. Rathinasuriyan, V. S. S. Kumar, Optimisation of submerged friction stir welding parameters of aluminium alloy using RSM and GRA, Adv. Mater. Process. Technol. 7 (2021) 696–709. https://doi.org/10.1080/2374068X.2020.1793264

[12] M. Tamjidy, B. Baharudin, S. Paslar, K. Matori, S. Sulaiman, F. Fadaeifard, Multi-objective optimization of friction stir welding process parameters of AA6061-T6 and AA7075-T6 using a Biogeography based optimization algorithm, Materials (Basel) 10 (2017) 533. https://doi.org/10.3390/ma10050533

[13] M. P. Alam, A. N. Sinha, Optimization of friction stir welding process parameters using desirability function analysis, Weld. Int. 36 (2022) 129–143. https://doi.org/10.1080/09507116.2022.2026745

[14] P. Kahhal, M. Ghasemi, M. Kashfi, H. Ghorbani-Menghari, J. H. Kim, A multi-objective optimization using response surface model coupled with particle swarm algorithm on FSW process parameters, Sci. Rep. 12 (2022) 2837. https://doi.org/10.1038/s41598-022-06652-3

[15] H. G. Nosrati, N. M. Yazdani, M. Khoran, Double-sided friction stir welding of AA 2024-T6 joints: Mathematical modeling and optimization, CIRP J. Manuf. Sci. Technol. 36 (2022) 1–11. https://doi:10.1016/j.cirpj.2021.10.010

[16] N. Chaudhary, S. Singh, Multi-objective optimization of friction stir spot welded Al 6061-T6 incorporated with silicon carbide using hybrid Grey Rational Analysis-Taguchi technique, Mater. Today Proc. (2022) (in press). https://doi.org/10.1016/j.matpr.2022.12.086

[17] M. H. Shojaeefard, R. A. Behnagh, M. Akbari, M. K. B. Givi, F. Farhani, Modelling and Pareto optimization of mechanical properties of friction stir welded AA7075/AA5083 butt joints using neural network and particle swarm algorithm, Mater. Des. 44 (2013) 190–198. https://doi.org/10.1016/j.matdes.2012.07.025

[18] P. Pankaj, A. Tiwari, P. Biswas, A. G. Rao, S. Pal, Experimental studies on controlling of process parameters in dissimilar friction stir welding of DH36 shipbuilding steel–AISI 1008 steel, Weld. World 64 (2020) 963–986. https://doi.org/10.1007/s40194-020-00886-3

[19] S. K. Gupta, K. Pandey, R. Kumar, Multi-objective optimization of friction stir welding process parameters for joining of dissimilar AA5083/AA6063 aluminum alloys using hybrid approach, Proc. Inst. Mech. Eng. Part L: J. Mater. Des. Appl. 232 (2018) 343–353. https://doi.org/10.1177/1464420715627294

[20] A. Premnath, Optimization of the process parameters on the mechanical and wear properties of Al-SiC nanocomposites fabricated by friction stir processing using desirability approach, Silicon 12 (2020) 665–675. https://doi.org/10.1007/s12633-019-00178-6

[21] N. Sharma, Z. A. Khan, A. N. Siddiquee, M. A. Wahid, Multi-response optimization of friction stir welding process parameters for dissimilar joining of Al6101 to pure copper using standard deviation based TOPSIS method, Proc. Inst. Mech. Eng. Part C: J. Mech. Eng. Sci. 233 (2019) 6473–6482. https://doi:10.1177/0954406219858628

[22] S. M. Haque, Optimized and validated Box–Behnken design combined response surface methodology to quantify acetic acid content in potassium clavulanate

using high-performance liquid chromatography, YJES 19 (2022) 50–61. https://doi:10.53370/001c.37877

[23] P. Cavaliere, R. Nobile, F. W. Panella, A. Squillace, Mechanical and microstructural behaviour of 2024–7075 aluminium alloy sheets joined by friction stir welding, Int. J. Mach. Tools Manuf. 46 (2006) 588–594. https://doi.org/10.1016/j.ijmachtools.2005.07.010

[24] Y. Motohashi, T. Sakuma, A. Goloborodko, T. Ito, G. Itoh, Grain refinement process in commercial 7075-T6 aluminum alloy under friction stir welding and super-plasticity, Materwiss. Werksttech. 39 (2008) 275–278. https://doi.org/10.1016/j.ijmachtools.2005.07.010

[25] K. Sithole, V. V. Rao, Recent developments in micro friction stir welding: A review, IOP Conf. Ser. Mater. Sci. Eng. 114 (2016) 012036. https://doi.org/10.1007/s11665-014-0968-x

[26] H. K. Rafi, G. D. J. Ram, G. Phanikumar, K. P. Rao, Microstructure and tensile properties of friction welded aluminum alloy AA7075-T6, Mater. Des. 31 (2010) 2375–2380. https://dx.doi.org/10.1016/j.matdes.2009.11.065

[27] M. Krishnan, S. K. Subramaniam, Investigation of mechanical and metallurgical properties of friction stir corner welded dissimilar thickness AA5086-AA6061 aluminium alloys, Mater. Res. 21 (2018). https://doi:10.1590/1980-5373-mr-2017-1045

[28] A. P. Tiwary, B. B. Pradhan, B. Bhattacharyya, Application of multi-criteria decision making methods for selection of micro-EDM process parameters, Adv. Manuf. 2 (2014) 251–258. https://doi:10.1007/s40436-013-0050-1

[29] S. Ramesh, R. Viswanathan, S. Ambika, Measurement, optimization of surface roughness and tool wear via grey relational analysis, TOPSIS and RSA techniques, Measurement 78 (2016) 63–72. https://doi:10.1016/j.measurement.2015.09.036

[30] S. Maniraj, R. Thanigaivelan, Optimization of electrochemical micromachining process parameters for machining of AMCs with different % compositions of GGBS using Taguchi and TOPSIS methods, Trans. Indian. Inst. Met. 72 (2019) 3057–3066. https://doi:10.1007/s12666-019-01772-3

[31] M. A. Herbert, A. K. Shettigar, A. V Nigalye, S. S. Rao, Investigation on microstructure and mechanical properties of Friction Stir Welded AA6061-4.5Cu-10SiC composite, IOP Conf. Ser. Mater. Sci. Eng. 114 (2016) 012125. https://doi:10.1088/1757-899x/114/1/012125

[32] S. Jeyakrishnan, S. Vijayakumar, M. Naga Swapna Sri, P. Anusha, An integration of RSM and ANN modelling approach for prediction of FSW joint properties in AA7178/AA5456 alloys, Canadian Metallurgical Quarterly (2024) 1–18. https://doi:10.1080/00084433.2024.2310344